

Prediction of Nontrivial Band Topology and Superconductivity in Mg_2Pb

Guang Bian,^{1*} Tay-Rong Chang,^{2*} Angus Huang,^{3,4*} Yuwei Li,¹ Horng-Tay Jeng,^{3,4} David J. Singh,¹ Robert J. Cava,⁵ and Weiwei Xie⁶

¹. Department of Physics and Astronomy, University of Missouri, Columbia, Missouri 65211, USA

². Department of Physics, National Cheng Kung University, Tainan, 701, Taiwan

³. Department of Physics, National Tsing Hua University, Hsinchu 30013, Taiwan

⁴. Institute of Physics, Academia Sinica, Taipei 11529, Taiwan

⁵. Department of Chemistry, Princeton University, Princeton, New Jersey 08544, USA

⁶. Department of Chemistry, Louisiana State University, Baton Rouge, Louisiana 70803, USA

Abstract

The interplay of BCS superconductivity and nontrivial band topology is expected to give rise to opportunities for creating topological superconductors, achieved through pairing spin-filtered boundary modes via superconducting proximity effects. The thus-engineered topological superconductivity can, for example, facilitate the search for Majorana fermion quasiparticles in condensed matter systems. Here we report a first-principles study of Mg_2Pb and predict that it should be a superconducting topological material. The band topology of Mg_2Pb is identical to that of the archetypal quantum spin Hall insulator HgTe , while isostructural and isoelectronic Mg_2Sn is topologically trivial; a trivial to topological transition is predicted for $\text{Mg}_2\text{Sn}_{1-x}\text{Pb}_x$ for $x \sim 0.77$. We propose that Mg_2Pb - Mg_2Sn quantum wells should generate robust spin-filtered edge currents in analogy to HgTe/CdTe quantum wells. In addition, our calculations predict that Mg_2Pb should become superconducting upon electron doping. Therefore, Mg_2Pb is expected to provide a practical material platform for studying emergent phenomena arising from the interplay of superconductivity and band topology.

*these authors equally contributed to this work.

Introduction

Recently, significant research effort had been devoted to the search for materials that incorporate both superconductivity and the topological band structure that is found in topological insulators (TIs)¹⁻⁴. The interplay of nontrivial band topology and superconductivity is expected to give rise to circumstances where time-reversal-invariant $p \pm ip$ superconductivity can naturally emerge as a consequence of the spin-momentum locking of topological surface electrons⁵. The surface $p \pm ip$ superconductivity in such superconductors would create a solid-state environment for realizing the Kitaev picture of Majorana fermions⁶. Several materials hosting both nontrivial band topology and superconductivity have been discovered and synthesized experimentally⁷⁻²⁰. Generally, these materials belong to two categories. The first are artificially fabricated TI/superconductor heterostructures in which superconductivity is introduced into TI films through superconducting proximity effects^{5,18,20}. The others are doped topological insulators that become superconducting themselves below a critical temperature^{8,9,13,16,21}. Although superconductivity has been found in these topological materials, new systems can be expected to display different characteristics. Therefore, there is a need for the identification of new topological superconductors. In this paper, we show by using first-principles calculations that dimagnesium plumbide, Mg_2Pb , is expected to be a BCS-type superconductor on electron doping, and, at same time, possesses a simple topological band structure that resembles that of the quantum spin Hall parent compound HgTe ²². Further a racial to topological transition is predicted for the $\text{Mg}_2\text{Pb}_{1-x}\text{Sn}_x$ system. Our theoretical results indicate that Mg_2Pb provides a promising alternative material path to search for topological superconductivity and Majorana quasiparticles in condensed matter systems.

Results and Discussion

Mg_2Pb crystallizes in a cubic anti-fluoride structure in which Pb atoms form a face-centered cubic (FCC) arrangement and the magnesium atoms occupy the eight tetrahedral voids, as shown in Fig. 1(a). The cubic lattice constants (in space group $Fm\bar{3}m$, # 225) are 6.815 Å and 6.776 Å for Mg_2Pb and the isostructural compound Mg_2Sn , respectively²³⁻²⁵. Figure 1(b) shows the first Brillouin zone of a FCC lattice with the high symmetry k points marked. The calculated bulk band structure of Mg_2Pb , obtained here using the generalized gradient approximation (GGA) method with the inclusion of spin-orbit coupling (SOC) is shown in Fig. 1(c). The Fermi surface is predominantly comprised of a hole pocket around Γ and an electron pocket around L. The calculated density of states indicates that the Pb-6*p* and Mg-3*s* orbitals dominate the conduction and valence bands close to the Fermi energy E_F . The overall band dispersion of Mg_2Pb is closely analogous to that of the archetypal quantum spin Hall compound mercury telluride (HgTe) except that the conduction band along Γ -L dives down to the Fermi level, forming an electron pocket at L. In contrast to the point-like Fermi surface of HgTe ²⁶, the Fermi surface of Mg_2Pb is large enough to allow for an effective Cooper pairing instability for low-energy electrons. Stoichiometric Mg_2Pb was reported to be superconducting in an old compilation²⁷, but that report was in error.

We now focus on the symmetry and topology of the Mg_2Pb band structure. Figure 2(a) shows the orbital decomposition of each energy band into Pb-6*p* and Mg-3*s* orbitals, which constitute the dominant low-energy electronic states. There are three sets of bands close to the Fermi level

of Mg_2Pb . For convenience, we employ the representation notation of HgTe to label the three relevant bands of Mg_2Pb ^{26,28}, because the two compounds essentially share the same band topology. As marked in Fig. 2(a), States Γ_6 , Γ_7 , and Γ_8 are two-, two-, and fourfold degenerate at Γ , and the Γ_8 state splits into two branches as it disperses away from Γ due to reduced symmetry. Each branch is doubly degenerate due to the presence of time-reversal and space inversion symmetries. The Γ_8 states lie above the Fermi level at Γ . The hole-like branch of Γ_8 is primarily derived from $\text{Pb-}6p$ orbitals while the electron-like branch evolves gradually from $\text{Pb-}6p$ to $\text{Mg-}3s$ with \mathbf{k} moving away from Γ . The Γ_6 band grazes the Fermi level at Γ . In contrast to Γ_8 , the Γ_6 state at Γ originates from the $\text{Mg-}3s$ orbital. This leads to a discrepancy in parity eigenvalue between Γ_6 and Γ_8 states. Our calculation shows that the parity eigenvalues are even and odd for Γ_6 and Γ_8 states, respectively. It is this ordering of bands with opposite parity eigenvalues that gives rise to a nontrivial band topology, analogous to what happens in HgTe . The hole-like Γ_7 band, mainly from $\text{Pb-}6p$ orbitals, is 1 eV below the Fermi energy and is irrelevant to the band topology near the Fermi energy.

The four-fold degeneracy of Γ_8 is protected by the C_4 symmetry of the lattice and therefore can be only lifted by a symmetry-breaking perturbation. In order to simulate a symmetry-breaking effect, we performed calculations where we compressed the cubic lattice by 3% along the cubic body diagonal direction, which is equivalent to increasing the angle α between FCC primitive lattice vectors from 60° to 61° . The resulting band structure is plotted in Fig. 2(b). Indeed, the C_4 -symmetry-breaking strain induces a gap of size 0.1 eV at the degenerate point of the Γ_8 band. With this gap, the conduction band is separated from the valence band throughout the whole Brillouin zone and, therefore, the topological Z_2 invariant can be calculated for this centrosymmetric compound by examining the parity eigenvalues of the valence band at time-reversal invariant momenta (TRIM) points²⁹. We find that the Z_2 invariant is $\nu = -1$, identical to that of strained HgTe and topological insulators, indicating that cubic Mg_2Pb has a topologically nontrivial band structure.

The defining characteristic of a topological insulator is the existence of topological surface states (TSS). To explore the surface states for Mg_2Pb , we calculated the band structure of a 30-unit cell undistorted cubic Mg_2Pb slab with a (110) surface. The result is shown in Fig. 2(c). The bands are plotted with the weight of the wavefunction on the top layer of the slab indicated in color, which makes it easy to discern the surface vs. bulk character of a state. Despite the absence of a bulk band gap at $\bar{\Gamma}$, a surface band is visible within a partial bulk band gap around the \bar{Y} point of the (110)-surface Brillouin zone. The surface band possesses a large Rashba spin splitting as a result of the broken space inversion symmetry at the surface and the strong atomic spin-orbit coupling (SOC) of the Pb atoms. We find that $E_R = 29.5$ meV, $k_0 = 0.063 \text{ \AA}^{-1}$ and $\alpha_R = 2E_R/k_0 = 0.93 \text{ eV}\cdot\text{\AA}$, which is comparable with some of the known bulk Rashba semiconductors such as BiTeI ($E_R = 100$ meV, $\alpha_R = 3.8 \text{ eV}\cdot\text{\AA}$) and BiTeCl ($E_R = 18.5$ meV, $\alpha_R = 1.2 \text{ eV}\cdot\text{\AA}$)³⁰⁻³². The Rashba point appears 0.4 eV below the Fermi level at \bar{Y} and the tails of the surface band merge into the bulk bands at $\bar{\Gamma}$. The vanishing bulk band gap in the undistorted material obscures a clear identification of the band topology. Lattice strains can exist in epitaxial films grown on substrates, however, which would lead to a desirable band gap at the degenerate point of the Γ_8 band^{26,33,34}. To simulate the strain effect, we calculated the electronic band structure of a semi-infinite Mg_2Pb -(110) slab with a 2% lattice compression along the (1-10)-direction, which

corresponds to $\bar{\Gamma} - \bar{X}$ in k space. The band structure along $\bar{\Gamma} - \bar{Y}$ colored with the surface weight of each state (Figs. 3(a, b)) shows that a band gap of about 30 meV is induced by such a strain, and that a Dirac surface band emerges inside the band gap in the same way as is the case for strained HgTe and α -Sn films³³⁻³⁷. The Dirac surface band traverses the band gap in the strained material in a gapless manner due to its topological origin. The topological character is further corroborated by inspecting the calculated spin texture of the surface band, which is shown in Figs. 3(c, d). The calculated dominant spin component of the surface states is S_X , which is in-plane and parallel to $\bar{\Gamma} - \bar{X}$. The other two spin components are found to be negligible. Therefore, the calculated spin polarizations of the Dirac surface states are perpendicular to the direction of the momentum, thus exhibiting a spin-momentum locking configuration which is characteristic of topological surface states.

Another way to visualize the topological nature of the Mg_2Pb band structure is to vary the effective SOC, a critical factor in this compound. Thus in Figures 4(a) and 4(b) we show the calculated band structures of Mg_2Pb without and with the inclusion of SOC. In the absence of SOC, the Γ_6 band lies above the Γ_8 band. The Γ_7 and Γ_8 bands are degenerate at Γ . When SOC is turned on, Γ_6 and Γ_8 are inverted in energy at Γ . The nontrivial band topology of Mg_2Pb arises from this band inversion. At the same time, Γ_7 is split off from Γ_8 by SOC, pushing Γ_7 to a higher energy region. The calculated bands for Mg_2Sn obtained similarly are presented in Figs. 4(c) and 4(d) for comparison. Since Sn is lighter than Pb, the atomic SOC of Mg_2Sn is weaker than that of Mg_2Pb . The band ordering of Mg_2Sn at the zone center is same as in the case of Mg_2Pb without SOC, that is Γ_6 is higher in energy than Γ_8 . Therefore, the energy difference $\Delta E = E_6(\Gamma) - E_8(\Gamma)$ is positive for Mg_2Sn but negative for Mg_2Pb . This change in sign signifies that Mg_2Sn belongs to a topologically distinctive topological phase. In other words, the band inversion and nontrivial topology of Mg_2Pb is induced by the strong SOC of the Pb atoms. Mg_2Sn and Mg_2Pb form an isostructural chemical pair with different band ordering, similar to the quantum spin Hall parent compounds HgTe and CdTe. The effective SOC can be tuned by varying the chemical composition in $\text{Mg}_2\text{Sn}_{1-x}\text{Pb}_x$. At the critical composition x_c , the band gap vanishes, and a topological phase transition occurs. Figure 4(e) presents the bulk energy gap as a function of Pb concentration x calculated via a mixed pseudopotential method³⁸. The critical concentration for the trivial to topological transition is found to be $x_c = 0.77$. The band structure at the critical point, presented in the upper panel of Fig. 4(e), shows the “touching” of Γ_6 and Γ_8 bands, and a linear bulk band dispersion, which is different from the symmetry-protected three-band crossings.³⁹ The system becomes a 3D Dirac semimetal at the critical point⁴⁰. The chemical and structural affinity between Mg_2Pb and Mg_2Sn , suggests that a quantum well heterostructure consisting of $\text{Mg}_2\text{Sn}/\text{Mg}_2\text{Pb}/\text{Mg}_2\text{Sn}$ with a variable well width, should achieve the quantum spin Hall effect with a robust spin-momentum-locked edge current, analogous to what has been done for CdTe/HgTe/CdTe quantum wells²². What makes Mg_2Pb different from HgTe is that with electron doping Mg_2Pb may become a BCS-type superconductor.

In order to explore the possible existence of superconductivity in Mg_2Pb , we performed systematic calculations for the electron-phonon coupling. Figure 5(a) shows the calculated phonon spectrum of undoped cubic Mg_2Pb , in which the magnitude of the calculated electron-phonon coupling λ_{qv} is indicated by the size of red dots. In our calculations, we find the total electron-phonon coupling $\lambda = \sum_{qv} \lambda_{qv}$ to be 0.239. The major contribution to λ comes from the acoustic phonon mode with lowest energy. Using the McMillan formula (see Method section for

details), the superconducting transition temperature T_c is estimated to be 0.002K for pure Mg_2Pb , an extremely low temperature. Mg_2Sn is not calculated to be superconducting at all. Our calculations show, however, that λ and T_c increase significantly when doping Mg_2Pb with electrons (or, equivalently, raising the Fermi level). The calculated relation between the electron doping and the Fermi level shift is illustrated in Fig. 5(b), where negative values of electron doping correspond to hole doping. We calculated λ and T_c at several doping levels as marked in the band structure shown in Fig. 5(c). The results in Fig. 5(d) suggest a monotonic increase of the superconducting critical temperature on raising the Fermi level. For example, when adding 0.7 electrons to the unit cell, T_c is calculated to become approximately 1.4 K. This effect becomes more prominent when the Fermi level shift is larger than 0.4 eV. Even in the event that the superconducting critical temperature is not accurately estimated in the calculations, the relative increase of T_c by a factor of $1.4/0.002 \sim 700$ on electron doping of Mg_2Pb may bring any superconducting transition in this system into an experimentally observable temperature range. On electron doping, the Fermi level is close to the band edge of the two Γ_8 branches, so the enhancement of superconductivity is likely due to the participation of electrons from the Γ_8 band edge and the electron-like Γ_8 band in the superconducting Cooper pairing. Electron doping also should also make possible the placing of the Fermi level inside the topological band gap of a strained Mg_2Pb film, in turn pairing the topological surface electrons through an effective surface-bulk proximity effect⁴¹. Therefore, this coincidence between the Fermi level shift and the strain-induced topological band gap is predicted to give rise to a potential visualization of helical $p \pm ip$ superconductivity on the surface of Mg_2Pb ¹⁸. Hole doping, by contrast, cannot promote the superconductivity in the compound.

Conclusion

In summary, we have investigated electronic structure and electron-phonon coupling of Mg_2Pb and Mg_2Sn by first-principles calculations. Our calculations reveal that Mg_2Pb should be a BCS-type superconductor upon electron doping, and at the same time possesses a nontrivial electronic band topology thanks to the strong spin-orbit coupling of Pb atoms. On the other hand, Mg_2Sn is calculated to be topologically trivial with a band ordering identical to that of CdTe. The calculated coexistence of nontrivial band topology and superconductivity makes Mg_2Pb a promising material for hosting topological superconductivity. There are two ways to visualize the topological superconductivity in Mg_2Pb . The first way is to create an $Mg_2Sn/Mg_2Pb/Mg_2Sn$ quantum well heterostructure, as has been done for CdTe/HgTe/CdTe quantum wells. By controlling the width of the quantum well, one may be able to tune the system into the quantum spin Hall phase and thus generate a pair of spin-momentum-locked topological edge bands. Because Mg_2Pb is calculated to be superconducting on electron doping, the edge state electrons may pair up through superconducting proximity effects to create a 1D $p \pm ip$ superconductor. The other approach would be to shift the Fermi level to the energy of the Dirac surface states in a strained Mg_2Pb film by substitutional alloying or applying a gating voltage. The spin-polarized surface electrons may then form Cooper pairs facilitated by the superconducting bulk-surface proximity effect, and, thus, generate a 2D topological $p \pm ip$ superconductor, which is line with the Fu-Kane mechanism of proximity-effect induced p-wave superconductivity⁵. Taking collectively our results on calculated band topology and superconductivity, we propose that Mg_2Pb provides a versatile platform for a material realization of topological superconductivity, especially in low dimensions. In addition, we calculate that by tuning the composition in Mg_2Sn_1 .

$x\text{Pb}_x$ to the critical value, one can potentially obtain a superconducting Dirac semimetal with a linear band dispersion, therefore opening a door for studying the rich physics arising from the interplay between superconductivity and Dirac semimetallic states.

Methods

We computed electronic structures using the projector augmented wave method^{42,43} as implemented in the VASP package⁴⁴⁻⁴⁶ within the generalized gradient approximation (GGA)⁴⁷ schemes. Experimental lattice constants were used and Monkhorst-Pack k -point meshes were used in the bulk and slab calculations, respectively. The spin-orbit coupling effects are included self-consistently.

The electron-phonon coupling, λ_{qv} is computed based on density functional perturbation theory⁴⁸ implemented in the Quantum Espresso code⁴⁹, using

$$\lambda_{qv} = \frac{1}{\pi N_F} \frac{\Pi''_{qv}}{\omega_{qv}^2} \quad (1)$$

Where N_F is the density of states (DOS) at the Fermi level, and λ_{qv} is the phonon frequency of mode v at wave vector \mathbf{q} . The electron-phonon quasiparticle linewidth, Π''_{qv} , is given by

$$\Pi''_{qv} = \pi \omega_{qv} \sum_{mn,k} |g_{mn}^v(\mathbf{k}, \mathbf{q})|^2 \delta(\epsilon_{nk}) \delta(\epsilon_{mk+\mathbf{q}}) \quad (2)$$

Where ϵ_{nk} is the energy of the KS orbital and the dynamical matrix reads:

$$g_{mn}^v(\mathbf{k}, \mathbf{q}) = \left(\frac{\hbar}{2M\omega_{qv}}\right)^{1/2} \left\langle \psi_{nk} \left| \frac{dV_{scf}}{d\mathbf{u}_{qv}} \cdot \hat{\mathbf{e}}_{qv} \right| \psi_{mk+\mathbf{q}} \right\rangle \quad (3)$$

Where $\frac{dV_{scf}}{d\mathbf{u}_{qv}}$ represents the deformation potential at the small atomic displacement $d\mathbf{u}_{qv}$ of the given phonon mode. M and $\hat{\mathbf{e}}_{qv}$ denote the mass of the atom and the unit vector along \mathbf{u}_{qv} , respectively. The critical temperature T_c can then be estimated by McMillan formula:

$$T_c = \frac{\omega_{ln}}{1.20} \exp \left[-\frac{1.04(1+\lambda)}{\lambda - \mu^*(1+0.62\lambda)} \right], \quad (4)$$

where

$$\lambda = \sum_{qv} \lambda_{qv} \quad (5)$$

$$\omega_{ln} = \exp \left[\frac{2}{\lambda} \int d\omega \frac{\ln \omega}{\omega} \alpha^2 F(\omega) \right] \quad (6)$$

$$\alpha^2 F(\omega) = \frac{1}{2} \int_{BZ} d\omega \lambda_{qv} \omega_{qv} \delta(\omega - \omega_{qv}) \quad (7)$$

$$\mu^* = 0.1 \quad (8)$$

Acknowledgements

GB acknowledges financial support from University of Missouri, Columbia. DJS and YL were supported by DOE through the computational materials science MAGICS center, DE-SC0014607. The work at Princeton University was supported by the ARO MURI on topological insulators, grant W911NF-12-1-0461. WX was supported by the LSU-startup funding. TRC was supported by the Ministry of Science and Technology and National Cheng Kung University, Taiwan. HTJ was supported by the Ministry of Science and Technology, National Tsing Hua University, and Academia Sinica, Taiwan. TRC and HTJ also thank NCHC, CINC-NTU, and NCTS, Taiwan for technical support.

Author Contribution

WX and GB searched for the materials candidates and designed the research; GB, TRC, AH, WX, HTJ YL and DJS conducted the computational work and RJC contributed to the analysis of the results. WX supervised the research. All authors contributed to the paper writing.

References

1. Hasan, M. Z. & Kane, C. L. Colloquium: Topological insulators, *Rev. Mod. Phys.* **82**, 30453067 (2010).
2. Qi, X-L. & Zhang, S.-C. Topological insulators and superconductors, *Rev. Mod. Phys.* **83**, 10571110 (2011).
3. Hasan, M. Z., Xu, S.-Y. & Bian, G. Topological insulators, topological superconductors and Weyl fermion semimetals: discoveries, perspectives and outlooks, *Phys. Scr.* **T164**, 014001 (2015).
4. Cava, R. J., Ji, H., Fuccillo, M. K., Gibson, Q. D., & Hor, Y. S. Crystal structure and chemistry of topological insulators. *J. Mater. Chem. C* **1(19)**, 3176-3189. (2013).
5. Fu, L. & Kane, C. L. Probing Neutral Majorana Fermion Edge Modes with Charge Transport, *Phys. Rev. Lett.* **102**, 216403 (2009).
6. Kitaev, A. Unpaired Majorana Fermions in Quantum Wires, *Physics Uspekhi* **44**, 131 (2001).
7. Ali, M. N., Gibson, Q. D. Klimczuk, T. & Cava, R. J. Noncentrosymmetric superconductor with a bulk three-dimensional Dirac cone gapped by strong spin-orbit coupling. *Phys. Rev. B* **89**, 020505(R) (2014).
8. Guang, B. *et al.* Topological Nodal-line Fermions in Spin-Orbit Metal PbTaSe₂, *Nat. Commun.* **7**,10556 (2016).
9. Neupane, M. *et al.* Observation of the spin polarized surface state in a noncentrosymmetric superconductor BiPd, *Nat. Commun.* **7**:13315 (2016).
10. Chang, C.-Z. *et al.* Experimental observation of the quantum anomalous Hall effect in a magnetic topological insulator, *Science* **340**, 167 (2013).
11. Wang, Z. F. *et al.* Topological Edge States in High-Temperature Superconductor FeSe/SrTiO₃(001) Film, *Nat. Mat.* **15**, 968 (2016).
12. Fu, L. & Berg E. Odd-Parity Topological Superconductors: Theory and Application to Cu_xBi₂Se₃, *Phys. Rev. Lett.* **105**, 097001 (2011).
13. Wray, L. A. *et al.* Observation of topological order in a superconducting doped

- topological insulator, *Nat. Phys.* **6**, 855 (2010).
14. Hor, Y. S. *et al.* Superconductivity in $\text{Cu}_x\text{Bi}_2\text{Se}_3$ and its implications for pairing in the undoped topological insulator, *Phys. Rev. Lett.* **104**, 057001 (2010).
 15. Sasaki, S. *et al.* Topological superconductivity in $\text{Cu}_x\text{Bi}_2\text{Se}_3$, *Phys. Rev. Lett.* **107**, 217001 (2011).
 16. Wang, Z., Taskin, A. A., Frolich, T., Braden, M., & Ando, Y. Superconductivity in $\text{Tl}_{0.6}\text{Bi}_2\text{Te}_3$ Derived from a Topological Insulator, *Chem. Mater.* **28**, 779 (2016).
 17. Hart, S. *et al.* Controlled finite momentum pairing and spatially varying order parameter in proximitized HgTe quantumwells, *Nat. Phys.* **13**, 87–93 (2017).
 18. Xu, S.-Y. *et al.* Momentum-space Imaging of Cooper Pairing in a Half-Dirac-gas Topological Superconductor. *Nat. Phys.* **10**, 943 (2014).
 19. Sun, H.-H. *et al.* Majorana Zero Mode Detected with Spin Selective Andreev Reection in the Vortex of a Topological Superconductor, *Phys. Rev. Lett.* **116**, 257003 (2016).
 20. Wang, E. *et al.* Fully gapped topological surface states in Bi_2Se_3 films induced by a d-wave high-temperature superconductor, *Nat. Phys.* **9**, 621 (2013).
 21. Han, C. Q. *et al.* Electronic structure of a superconducting topological insulator Sr-doped Bi_2Se_3 , *Appl. Phys. Lett.* **107**, 171602 (2015).
 22. König, M. *et al.* Quantum Spin Hall Insulator State in HgTe Quantum Wells, *Science* **318**, 766-770 (2007).
 23. Faessler, T. F. & Kronseder, C. Single Crystal Structure Refinement of Dimagnesium Plumbide, Mg_2Pb , *Z. Kristallogr. - New Cryst. Struct.* **214**, 438-438 (1999).
 24. Nikitin, E. N., Tkalenko, E. N., Zaitsev, V. K., Zaslavskii, A. I., & Kuznetsov, A. K. A study of the phase diagram for the Mg_2Si - Mg_2Sn system and the properties of certain of its solid solutions, *Inorganic Materials* **4**, 1656-1659 (1968).
 25. Li, Y., Bian, G. & Singh, D. J. Identification and properties of the non-cubic phases of Mg_2Pb , *AIP Advances* **6**, 125108 (2016).
 26. Liu, C. *et al.* Tunable spin helical Dirac quasiparticles on the surface of three-dimensional HgTe, *Phys. Rev. B* **92**, 115436 (2015).
 27. Roberts, B. W. Survey of superconductive materials and critical evaluation of selected properties *J. Phys Chem. Ref. Data* **5**, 581-794 (1976).
 28. Ren, J. *et al.* Electronic structure of the quantum spin Hall parent compound CdTe and related topological issues, *Phys. Rev. B* **90**, 205211 (2014).
 29. Fu, L. & Kane, C. L. Topological insulators with inversion symmetry, *Phys. Rev. B* **76**, 045302 (2007).
 30. Ast, C. *et al.* Giant Spin Splitting through Surface Alloying, *Phys. Rev. Lett.* **98**, 186807 (2007).
 31. Xiang, F.-X. *et al.* Observation of topological transition of Fermi surface from a spindle torus to a torus in bulk Rashba spin-split BiTeCl , *Phys. Rev. B* **92**, 035123 (2015).
 32. Ishizaka, K. *et al.* Giant Rashba-type spin splitting in bulk BiTeI , *Nat. Mater.* **10**, 521 (2011).
 33. Han, H., Zhang, Y., Gao, G. Y. & Yao, K. L. The lattice distortion-induced topological insulating phase in bulk HgTe from first-principles, *Solid State Commun.* **153**, 31 (2013).
 34. Brüne, C. *et al.* Quantum Hall Effect from the Topological Surface States of Straine Bulk HgTe, *Phys. Rev. Lett.* **106**, 126803 (2011).
 35. Kirtschig, F., van den Brink, J. & Ortix C., Surface-state spin textures in strained bulk HgTe: Strain-induced topological phase transitions, *Phys. Rev. B* **94**, 235437 (2016).

36. Ohtsubo, Y., P. Le Fevre, F. B. & Taleb-Ibrahimi A. Dirac Cone with Helical Spin Polarization in Ultrathin α -Sn(001) Films, *Phys. Rev. Lett.* **111**, 216401 (2013).
37. Wu, S.-C., Yan, B. & Felser, C. Ab initio study of topological surface states of strained HgTe, *EPL* **107**, 57006 (2014).
38. Bian, G., Wang, X., Miller, T. & Chiang, T.-C. Topological phase transition and Dirac fermion transfer in Bi₂Se₃ films, *Europhys. Lett.* **101**, 27004 (2013).
39. Bradlyn, B. *et al.* Beyond Dirac and Weyl fermions: Unconventional quasiparticles in conventional crystals. *Science* **353**:6299, aaf5037 (2016).
40. Wang, Z. *et al.* Dirac semimetal and topological phase transitions in A₃Bi (A=Na, K, Rb), *Phys. Rev. B* **85**, 195320 (2012).
41. Xu, S.-Y *et al.* Topological phase transition and texture inversion in a tunable topological insulator. *Science* **332**:6029, 560 (2011).
42. Blöchl, P. E. Projector augmented-wave method, *Phys. Rev. B.* **50**, 17953 (1994).
43. Kresse, G. & Joubert, J. Ultrasoft pseudopotentials to the projector augmented-wave method, *Phys. Rev. B.* **59**, 1758 (1999).
44. Kress, G. & Hafner, J. Ab initio molecular dynamics for open-shell transition metals, *Phys. Rev. B.* **48**, 13115 (1993).
45. Kress, G. & Furthmüller, J. Efficiency of ab-initio total energy calculations for metals and semiconductors using a plane-wave basis set, *Comput. Mater. Sci.* **6**, 15 (1996)
46. Kress, G. & Furthmüller, J. Efficient iterative schemes for ab initio total-energy calculations using a plane-wave basis set, *Phys. Rev. B.* **54**, 11169 (1996).
47. Perdew, J. P., Burke, K. & Ernzerhof, M. Generalized Gradient Approximation Made Simple, *Phys. Rev. Lett.* **77**, 3865 (1996).
48. Baroni, S., de Gironcoli, S., Dal Corso, A. & Giannozzi, P. Phonons and related crystal properties from density-functional perturbation theory, *Rev. Mod. Phys.* **73**, 515 (2001).
49. Giannozzi, P. *et al.* QUANTUM ESPRESSO: A Modular and Open-source Software Project for Quantum Simulations of Materials, *J. Phys. Condens. Matter* **21**, 395502 (2009).

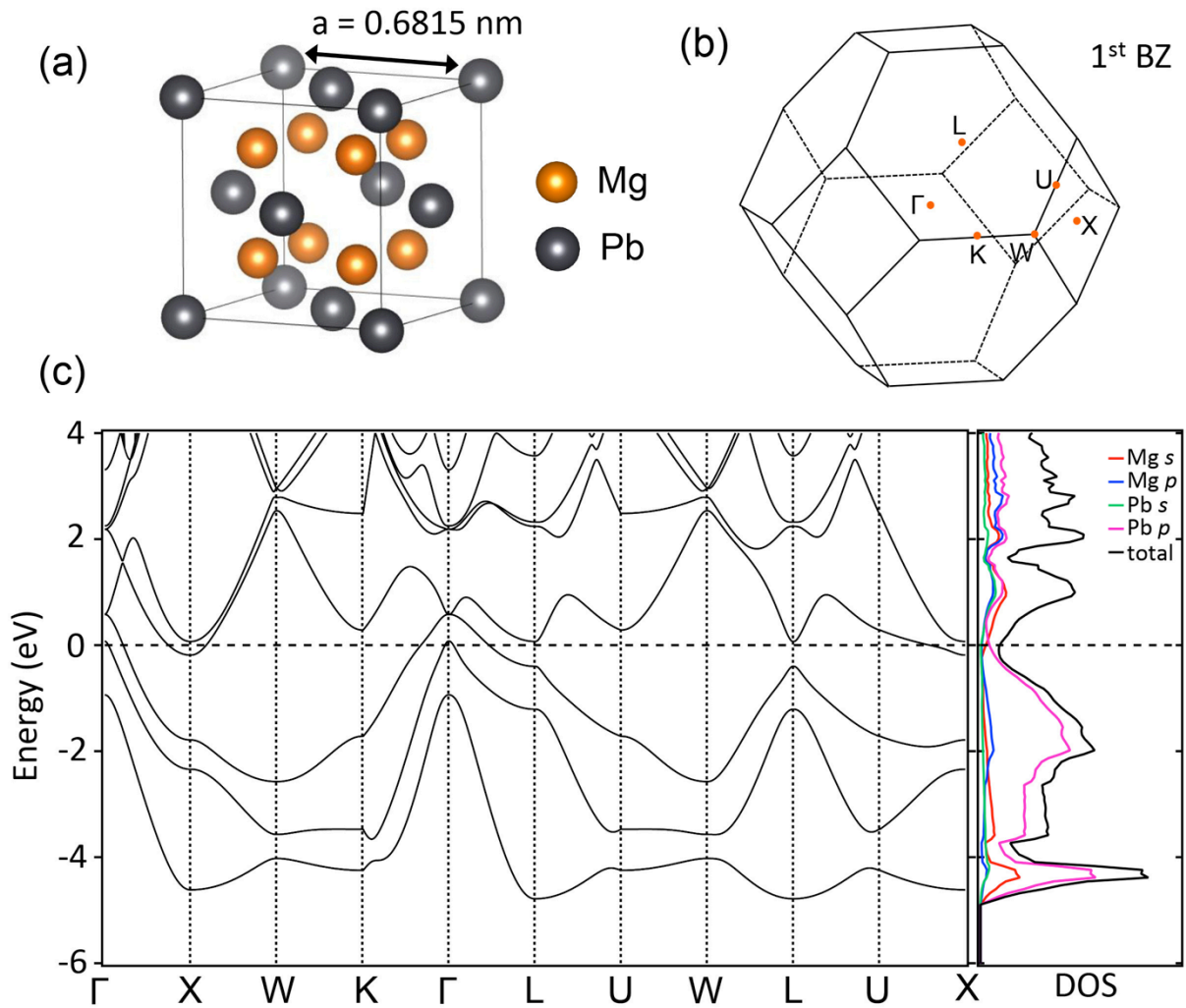


Figure 1. (a) The cubic anti-fluorite lattice structure of undistorted Mg_2Pb . (b) The first Brillouin zone with high symmetry points indicated. (c) Bulk band structure and density of states (DOS) of cubic Mg_2Pb using the method of generalized gradient approximation (GGA). The spin-orbit coupling (SOC) is taken into account in the calculation. The orbital-projected DOS curves are plotted in color.

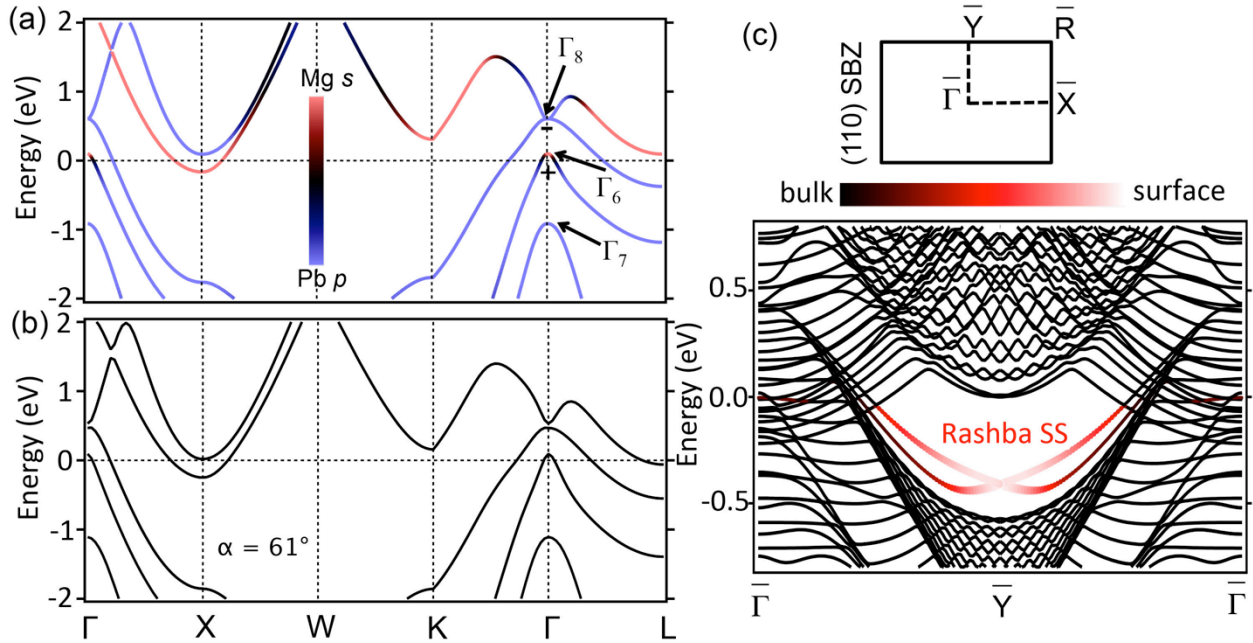


Figure 2. (a) Band structure of cubic undistorted Mg_2Pb with orbital projection onto Mg-s and Pb-p orbitals. The color bar gives the projection weight. The symmetry of each band is denoted by Γ_i ($i = 6; 7; 8$). The '+' and '-' signs indicate the parity eigenvalues of corresponding states. (b) The bulk band structure of distorted Mg_2Pb with a strain compressing the cubic lattice along the body diagonal direction by 3 percent. The angle between FCC primitive vectors is increased from 60° to 61° by the strain. (c) Band structure of an undistorted 30-unit-cell Mg_2Pb -(110) slab and the surface Brillouin zone. $\bar{\Gamma} - \bar{X}$ and $\bar{\Gamma} - \bar{Y}$ correspond to the (1-10) and (001) directions, respectively. The bands are colored according to the weight of wavefunction on the top layer of the slab.

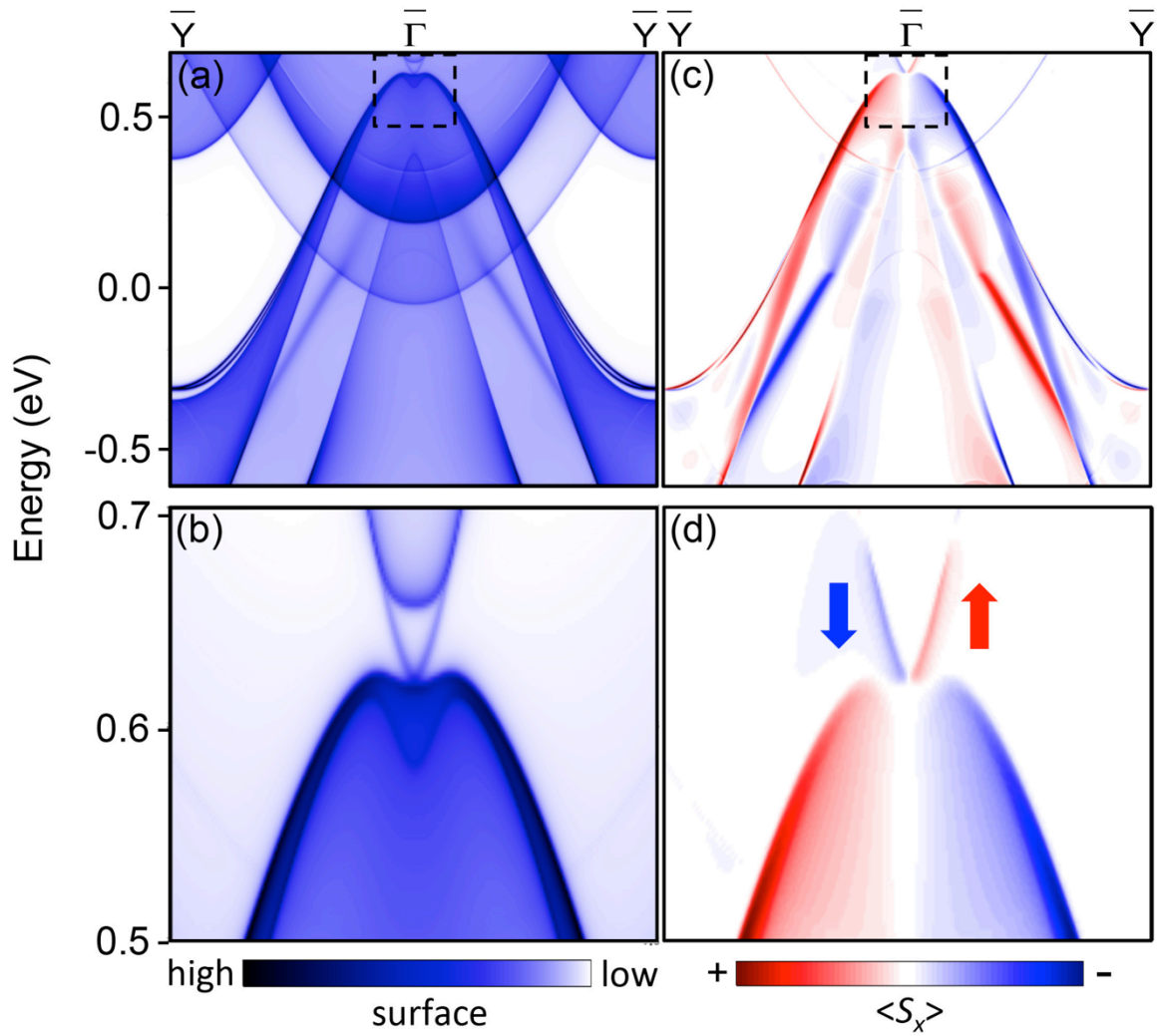


Figure 3. (a) Calculated band structure of a semi-infinite Mg_2Pb -(110) slab with a 2% lattice compression along the (1-10) direction. The depth of blue color shows the surface weight of each wave function. (b) Zoom-in of the part of the electronic band structure enclosed by the dashed rectangle in (a). (c and d) Spin polarization of bands shown in red and blue. The spin is aligned primarily along S_x , i.e., the spin is in-plane and perpendicular to the direction of momentum. The other two components of spin are negligibly small.

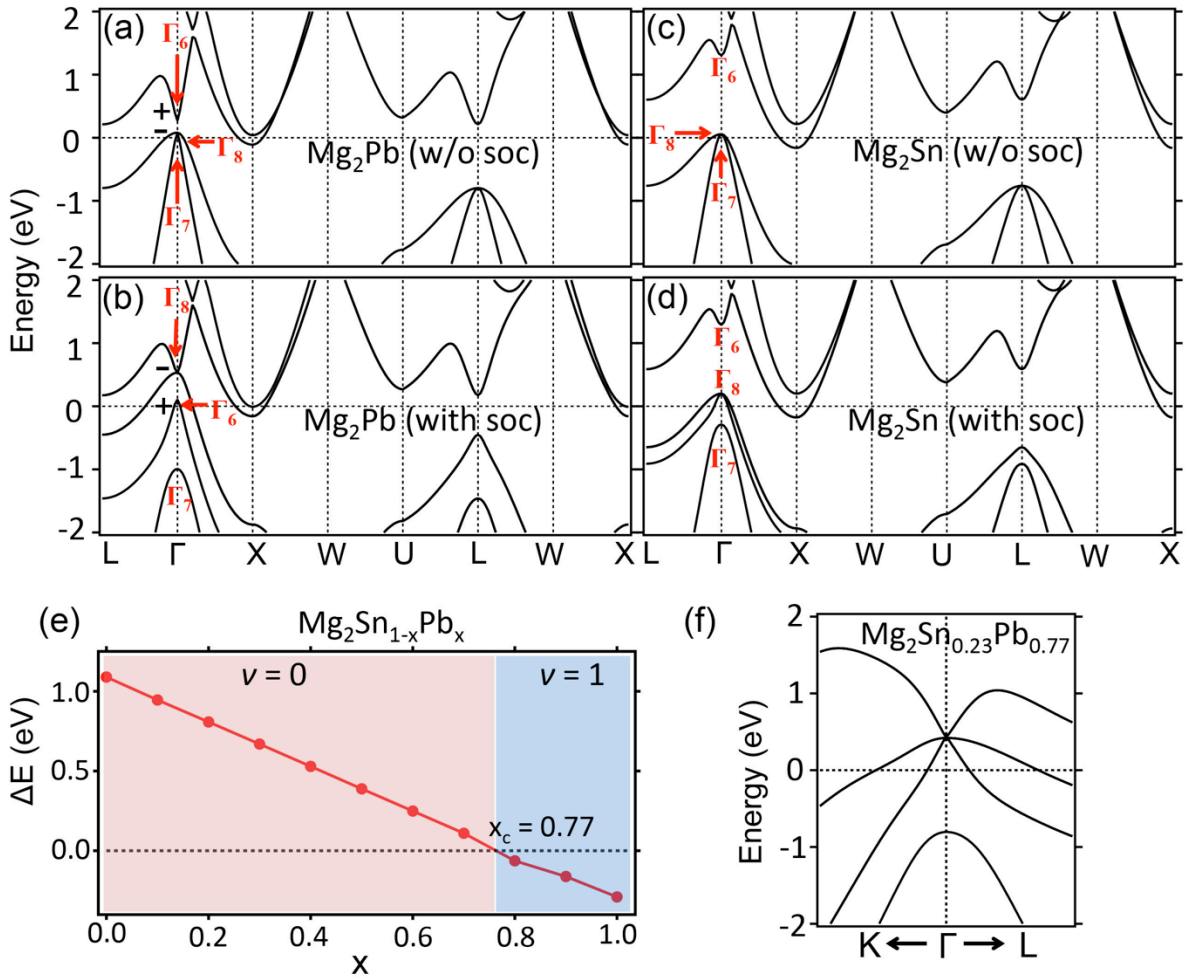


Figure 4. Calculated band structure of (a) undistorted cubic Mg_2Pb without SOC, (b) same for Mg_2Pb with SOC, (c) Mg_2Sn without SOC, and (d) Mg_2Sn with SOC. (e) The phase diagram of $\text{Mg}_2\text{Sn}_{1-x}\text{Pb}_x$ with the bulk band gap as a function of the composition x . The critical composition is $x_c = 0.77$. (f) The band structure of $\text{Mg}_2\text{Sn}_{1-x}\text{Pb}_x$ at $x_c = 0.77$.

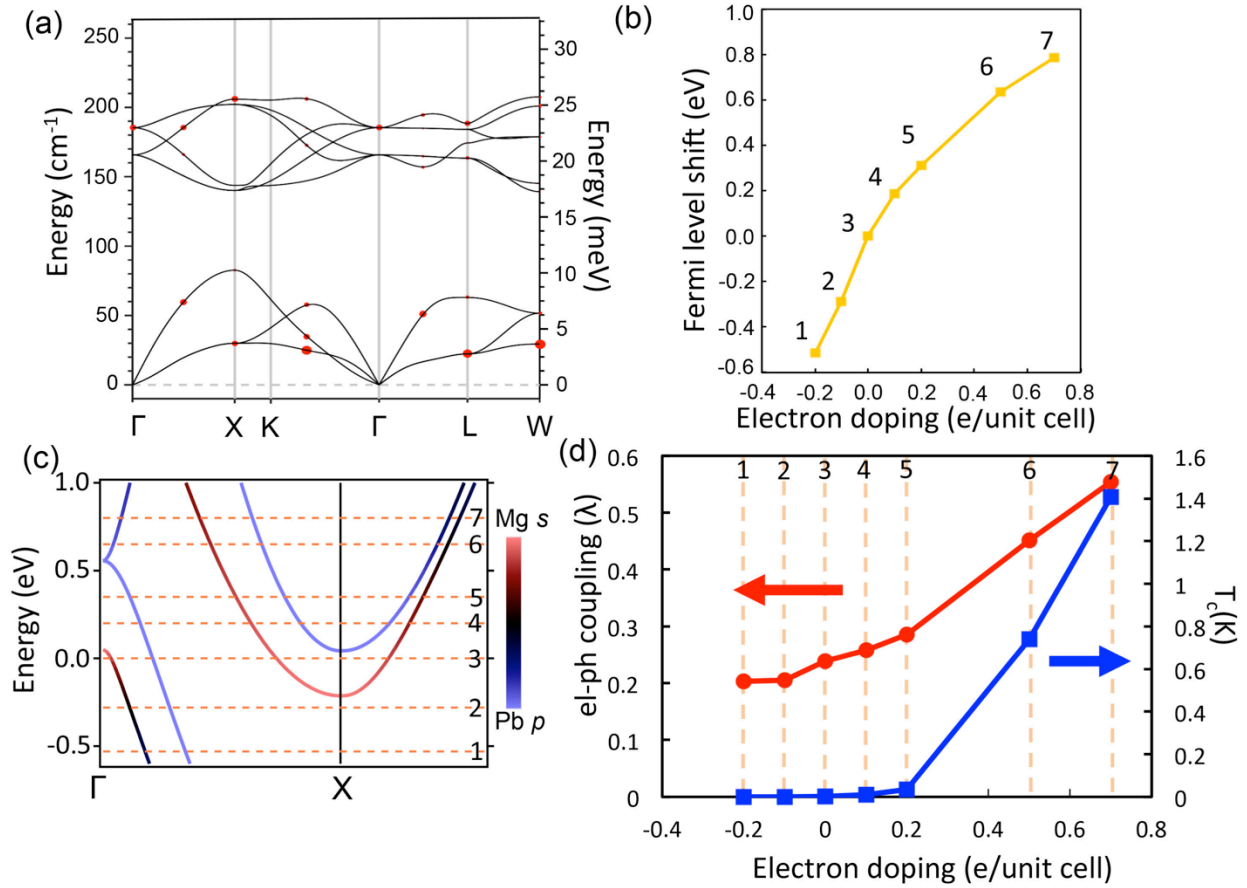


Figure 5. (a) calculated Phonon dispersion for cubic Mg₂Pb. The size of red dots indicates the magnitude of the electron-phonon coupling λ_{qv} at different places in the Brillion Zone (b) The dependence of Fermi level shift on electron doping. (c) The band structure of Mg₂Pb. The energies marked by the dashed lines correspond to the results in (b, d) with same labels. (d) The calculated superconducting critical temperature T_c and effective electron-phonon coupling λ_{qv} of Mg₂Pb as a function of electron doping concentration.